

GAIR: Improving Multimodal Geo-Foundation Model with Geo-Aligned Implicit Representations

Zeping Liu¹, Fan Zhang², Junfeng Jiao¹, Ni Lao^{*1}, and Gengchen Mai^{*1}

¹The University of Texas at Austin, {zeping.liu, jjiao, nlao, gengchen.mai}@utexas.edu

²Peking University, fanzhanggis@pku.edu.cn

Abstract

Advancements in vision and language foundation models have inspired the development of geo-foundation models (GeoFMs), enhancing performance across diverse geospatial tasks. However, many existing GeoFMs primarily focus on overhead remote sensing (RS) data while neglecting other data modalities such as ground-level imagery. A key challenge in multimodal GeoFM development is to explicitly model geospatial relationships across modalities, which enables **generalizability across tasks, spatial scales, and temporal contexts**. To address these limitations, we propose GAIR, a novel multimodal GeoFM architecture integrating overhead RS data, street view (SV) imagery, and their geolocation metadata. We utilize three factorized neural encoders to project an SV image, its geolocation, and an RS image into the embedding space. The SV image needs to be located within the RS image’s spatial footprint but does not need to be at its geographic center. In order to geographically align the SV image and RS image, we propose a novel implicit neural representations (INR) module that learns a continuous RS image representation and looks up the RS embedding at the SV image’s geolocation. Next, these geographically aligned SV embedding, RS embedding, and location embedding are trained with contrastive learning objectives from unlabeled data. We evaluate GAIR across 10 geospatial tasks spanning RS image-based, SV image-based, and location embedding-based benchmarks. Experimental results demonstrate that GAIR outperforms state-of-the-art GeoFMs and other strong baselines, highlighting its effectiveness in learning generalizable and transferable geospatial representations.

1. Introduction

In the geospatial domain, researchers usually have access to vast amounts of **unlabeled geospatial datasets** such as

*Corresponding Author.

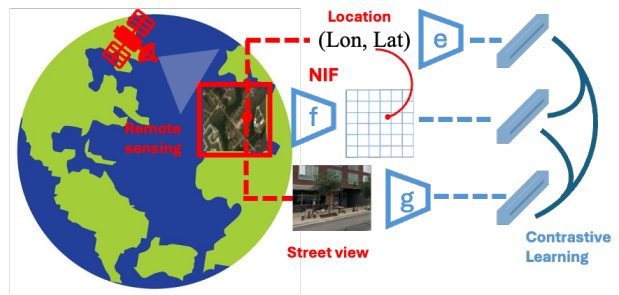


Figure 1. Overview of the proposed GAIR architecture, which encodes data of three geospatial modalities: street view image s_i , its geolocation coordinate x_i , and remote sensing image r_i . The **location encoder** e is an implicit function transforming geolocation x_i into a latent representation $e(x_i)$, while **Vision Transformer (ViT)-based image encoders** extract representations from remote sensing and street view images, denoted as $f(r_i)$ and $g(s_i)$, respectively. A novel **Implicit Neural Representation (INR)** module refines $f(r_i)$ into a localized embedding z_i^q , which is geographically aligned with $g(s_i)$ and $e(x_i)$. z_i , $g(s_i)$, and $e(x_i)$ are trained in a self-supervised manner through contrastive learning.

satellite images, street view images, and user-generated geo-tagged data (e.g., Flickr images, geo-tagged tweets, species images from the iNaturelist app, etc). In contrast, **labeled geospatial data** is typically scarce and highly imbalanced in terms of spatial, temporal, and class coverage [36, 46], due to the high cost of data annotation and the specialized domain expertise required. This scarcity of labeled data significantly limits the usage of these multimodal geospatial data in critical geospatial applications such as economic development prediction [35], species distribution modeling [14, 47], crop yield estimation [5, 79], urban dynamics monitoring [8], geographic question answering [43, 80], and climate extreme event detection [25]. Furthermore, training AI models on these limited labeled datasets restricts both their geographic [37, 38, 74] and task generalizability [15, 49].

Meanwhile, recent advancements in language and vision

foundation models – designed as pre-trained, task-agnostic models that can be adapted to excel across a wide range of downstream tasks with limited labels – have greatly inspired the development of geo-foundation models (GeoFMs) [30, 48] for geospatial applications, to tackle the issue of limited supervised information. However, *most existing GeoFMs are heavily oriented toward remote sensing (RS) tasks* [15, 24, 28], e.g., RSFMs, by leveraging massive unlabeled overhead RS images. While multiple multimodal geo-foundation models [3, 20] have been developed, they primarily focus on effectively integrating different modalities of overhead remote sensing data (e.g., optical, synthetic aperture radar (SAR) data, etc.) while overlooking other important geospatial data modalities such as ground-level images and geospatial vector data. This neglect of diverse datasets significantly limits the spatial reasoning capabilities of these models and hampers their generalizability across different tasks, regions, spatial scales, and temporal contexts. Furthermore, many GeoFMs mainly rely on conventional language and vision foundation model objectives like temporal or spatial augmented embeddings [24, 62] or image reconstruction [15, 33, 64], without explicitly considering the geospatial relationships between different data modalities, leading to suboptimal results for geospatial applications.

A key reason for the current emphasis on remote sensing-based GeoFMs is the challenge of aligning geospatial data across diverse spatial scales. Different geospatial modalities capture information at varying spatial scales. For instance, overhead satellite imagery provides a broad spatial contextual view, while street view (SV) images capture fine-grained ground-level details. A single 256×256 overhead RS image can correspond to hundreds or even thousands of SV images which makes it extremely difficult to create valuable geospatial-aligned RS-SV image pairs for the self-supervised learning (SSL) purpose. Traditional SSL paradigms [26, 27] struggle to effectively align these disparate scales effectively, hindering the integration of multimodal geospatial data.

In this paper, we argue that there is vast amounts of information naturally shared between ground-level and overhead views of a scene, by using geo-location as a bridge. Following this idea, we deploy neural implicit functions [13, 21, 60] to learn a continuous image representation from a remote sensing image and extract a neural representation that is geographically colocated with a ground-level image. By further projecting the ground-level image and its geolocation into an image embedding and a location embedding [36, 45, 46, 74] with respective neural encoders, we can form a self-supervised learning objective by performing multi-objects contrastive learning on these three colocated embeddings. Based on this spatially explicit contrastive learning framework, we develop a multimodal Geo-foundation model called GAIR. An overview of GAIR is provided in Figure 1. The contributions of this paper are as follows:

- We propose GAIR, a GeoFM capable of handling diverse geospatial modalities, including remote sensing imagery, street view imagery, and geo-location encoding. By integrating these modalities, GAIR provides a more comprehensive geospatial understanding.
- The design of GAIR involves three key technical components: a) Factorized multimodal encoder design allows the model to retain modality-specific information while effectively learning cross-modal relationships. b) Neural implicit functions learn continuous representations on RS images and extract fine-grained localized embeddings that are geographically co-located with ground-level images. c) Contrastive learning is applied to these geospatial aligned neural embeddings from three distinct modalities in order to learn generalizable geospatial representations across different tasks.
- We pre-train GAIR on a globally sampled dataset named **Streetscape1M** with 1 million samples. The pre-trained GAIR is adapted to a wide range of geospatial tasks via few-shot learning or full fine-tuning. Experimental results show that GAIR outperforms all baselines and achieves state-of-the-art (SOTA) performance across all 10 geospatial tasks including street view imagery tasks, remote sensing imagery tasks, and location embedding tasks.

2. Related Work

2.1. Geo-Foundation Models

Many recent Geo-Foundation Models draw inspiration from Vision Foundation Models [10–12, 16, 23, 27, 40, 55] and Vision-Language Models [57, 70, 81]. Unlike traditional vision datasets, geospatial data inherently integrates spatial and temporal information, requiring specialized model architectures. Current Geo-Foundation Models can be roughly categorized into (1) Remote Sensing Foundation Models (RSFMs) and (2) Weather and Climate Foundation Models. RSFMs leverage contrastive learning or masked image modeling (MIM) to learn task-agnostic neural representations. GASSL [4] and SeCo [50] use temporal augmentations with a MoCo v2 [26] self-supervised learning (SSL) objective, while Dino-MC [71] and Skysense [24] extend DINO [10] to multi-scale and multi-modal settings. SatMAE [15], CROMA [20], OmniSat [2], and DOFA [76] apply MIM for self-supervised learning on remote sensing imagery. Climate models such as ClimaX [54] was pre-trained on multi-source climate data using MIM. However, most existing models focus on a fixed spatial scale and overlook the integration of ground-level imagery and geospatial vector data, thus lacking precise spatial reasoning and understanding capabilities. Our work addresses these issues by integrating overhead imagery, street view imagery, and geolocation into the same SSL framework by using a spatially explicit contrastive learning objective.

2.2. Implicit Neural Representations

Implicit Neural Representations (INR) have been widely applied across various domains, including image regression [66], compression [18], 3D reconstruction [53], image super-resolution [13, 21], etc. The core idea behind INR is to learn a continuous function that maps spatial coordinates to corresponding signals, enabling flexible, resolution-independent data representation. A common approach is to transform spatial coordinates into multi-scale features using Fourier feature mappings [66], which are then processed by a multi-layer perceptron (MLP) to learn a continuous representation for downstream tasks. This technique has been particularly effective in image super-resolution such as LIIF [13] and CiaoSR [9], which directly learn pixel-wise feature mappings for image restoration.

In the geospatial domain, implicit neural representations have been utilized for POI type prediction [44], geo-aware species fine-grained recognition [42, 46, 47], species distribution modeling [14], image geolocalization [69], satellite image classification and regression [36, 74], and geographic question answering [43]. In this work, we use an INR-based location encoder to represent geolocations into the embedding space. In addition, a novel implicit neural representation module is proposed to refine the remote sensing representations $f(r_i)$ into a localized RS embedding $\hat{r}_i(x)$ that is geographically aligned with street view image embedding $g(s_i)$ and the location embedding $e(x_i)$. Three embeddings $-\hat{r}_i(x)$, $g(s_i)$, and $e(x_i)$ – are trained in a self-supervised manner through contrastive learning.

3. Methods

3.1. Factorized Encoder for Geospatial Modalities

We define an unlabeled geo-tagged image dataset as $X = \{(r_i, s_i, x_i) \mid i = 1, \dots, M\}$, where r_i is a remote sensing image, s_i a street view image and x_i the location (longitude and latitude) of s_i . Here, x_i is within the spatial footprint $A(r_i)$ of r_i but might not be the geometric center of r_i .

Inspired by recent contrastive pretraining models [24, 46, 57], we adopt a factorized encoder architecture to extract modality-specific features independently, as shown in Figure 2. Specifically, we introduce a remote sensing image encoder $f(\cdot)$, a street view image encoder $g(\cdot)$, and a location encoder $e(\cdot)$. This modular design allows each encoder to capture unique spatial and semantic characteristics potentially with pretrained encoders of that modality, while forming the bases of multimodal alignment in a later stage.

For image encoders, recent vision foundation models have demonstrated remarkable generalization across diverse computer vision tasks. Motivated by this, we employ two independent Vision Transformers (ViTs) [17] as our encoders: $f(\cdot)$ for remote sensing images and $g(\cdot)$ for street view images. For stable training, the remote sensing image encoder

$f(\cdot)$ is initialized with a pretrained RSFM checkpoint. To adapt the encoder for our multimodal contrastive training, we add one trainable linear projection layer with a dimension of D . Hence, our image encoders will generate two feature embeddings, $f(r_i)$ and $g(s_i)$.

The location encoder $e(\cdot)$ is defined as a function $e_\theta(\mathbf{x}_i) : \mathbb{S}^2 \rightarrow \mathbb{R}^d$, parameterized by θ , which maps any coordinate $\mathbf{x}_i = (\lambda_i, \phi_i)$ on the spherical surface \mathbb{S}^2 to a d -dimensional vector representation. Here, the longitude $\lambda_i \in [-\pi, \pi)$ and latitude $\phi_i \in [-\pi/2, \pi/2]$. We leverage existing 2D location encoders [74], specifically adopting Random Fourier Features (RFF) implemented from GeoCLIP [69], due to its strong performance in prior works. The location encoding is represented as $e(x_i)$.

3.2. Contrastive Objective

Given $e(x_i)$, $f(r_i)$, and $g(s_i)$, we can achieve generalizable representation learning by aligning these representations using geographic colocation information. Here, we mainly use two contrastive learning strategies.

Implicit Neural Contrastive Learning (INCL). Given an overhead RS image representation $f(r_i)$, we reshape it into a 2D feature map $f(r_i) \in \mathbb{R}^{P \times P \times D}$, where P^2 is the number of patches in the ViT backbone, preserving the spatial structure of the image. Each feature $f(r_i)_{ab}$ corresponds to a real-world geographic location via geo-referencing, representing every latent vector with a specific latitude-longitude coordinate, where a and b denote the row and column indices in the grid representation of $f(r_i)$. Through geo-referencing, these indices are mapped to real-world geographic coordinates. To extract an RS image embedding at the geolocation x_i of a street-view image s_i , we develop a novel INR module $\Omega(\cdot)$ on top of the output $f(r_i)$ of the ViT-based RS image encoder inspired by LIIF [13]. $\Omega(\cdot)$ can learn a continuous representation of an RS image and be able to extract image embeddings at any query geolocation $x_i^{(q)} \in A(r_i)$. This involves two critical steps:

- Feature Unfolding:** To enrich each latent feature with the local context, we apply a neighborhood expansion strategy, concatenating features from a 3×3 grid of neighboring RS image patches. This increases the receptive field and provides richer information for spatial interpolation. Please refer to Appendix A.1 for details.
- Local Ensemble Interpolation:** Instead of directly retrieving a single latent code $z_i^{(q)}$ at coordinate $x_i^{(q)}$ by using grid sample function [31], we generate $z_i^{(q)}$ by interpolating from the four nearest latent codes $z_i^{(k)}$ (top-left, top-right, bottom-left, bottom-right) at location $x_i^{(q)}$ to ensure smooth transitions across space:

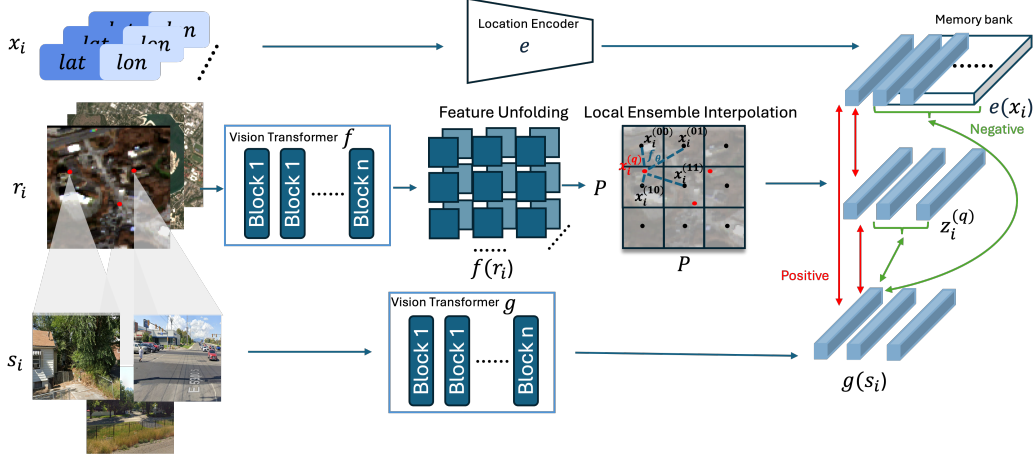


Figure 2. Overview of the proposed GAIR architecture, which encodes data of three geospatial modalities: geolocation coordinate x_i , remote sensing image r_i^t , and street view image s_i . The location encoder e transforms geolocation x_i into a latent representation $e(x_i)$, while ViT-based image encoders extract representations from remote sensing and street view images, denoted as $f(r_i)$ and $g(s_i)$, respectively. Implicit Neural Representation (INR) refines $f(r_i)$ into a localized embedding $z_i^{(q)}$ through feature unfolding and local ensemble interpolation. Then we do contrastive learning to align these three feature embeddings.

$$z_i^{(q)} = \Omega(f(r_i), x_i^{(q)}) \quad (1)$$

$$= \sum_{k \in \{00, 01, 10, 11\}} \frac{S_k}{S} \cdot f_{\theta}(z_i^{(k)}, x_i^{(q)} - x_i^{(k)}) \quad (2)$$

where $z_i^{(k)}$ ($k \in \{00, 01, 10, 11\}$) are the nearest latent codes of the four locations of image patches. $x_i^{(k)}$ denotes the spatial coordinate of $z_i^{(k)}$. S_k is the area of the rectangle formed between x_i^q and its corresponding surrounding coordinate $x_i^{(k)}$. f_{θ} is an MLP modulated by the latent code $z_i^{(k)}$ which takes the coordinate difference between $x_i^{(q)}$ and $x_i^{(k)}$ and predict the latent code $z_i^{(q)}$ at location x_i^q . Please refer to Appendix A.2 for details. The final interpolation weights are normalized by the total rectangle area S . This approach ensures local feature continuity by enabling overlapping representations from neighboring latent codes. At each query location, four independent predictions are generated and merged using normalized area-based voting, leading to smooth and spatially coherent feature synthesis.

Finally, the RS embedding $z_i^{(q)}$ at $x_i^{(q)}$ is contrastively aligned with the corresponding SV embedding $g(s_i)$:

$$\mathcal{L}_{\text{INCL}} = -\frac{1}{2N} \sum_{i=1}^N \left[\log \frac{\exp(\text{sim}(z_i^{(q)}, g(s_i))/\tau)}{\sum_{j=1}^N \exp(\text{sim}(z_i^{(q)}, g(s_j))/\tau)} + \log \frac{\exp(\text{sim}(g(s_i), z_i^{(q)})/\tau)}{\sum_{j=1}^N \exp(\text{sim}(g(s_i), z_j^{(q)})/\tau)} \right] \quad (3)$$

where $\text{sim}(\cdot, \cdot)$ denotes a cosine similarity function, N is the batch size, and τ is a temperature parameter. This contrastive loss enforces positive pairs between the matched embeddings

while discouraging alignment with non-matching locations [57]. The first term ensures that the synthesized RS embedding $z_i^{(q)}$ is aligned with the corresponding collocated SV embedding $g(s_i)$, while the second term enforces the inverse alignment, treating $g(s_i)$ as the anchor.

Spatially Explicit Contrastive Learning (SECL). To further reinforce the geospatial consistency across modalities, we introduce SECL, which incorporates explicit location encoding into the contrastive learning framework. Instead of aligning embeddings solely based on visual similarity, we integrate the location embedding $e(x_i)$ into the loss function to guide the alignment process.

We construct a memory bank \mathcal{M} [26, 69] to store location embeddings $e(x_i)$ from past mini-batches. The SECL objective consists of two separate contrastive losses: one aligning location embeddings with remote sensing features, and another aligning location embeddings with street view features. The total loss is defined as:

$$\mathcal{L}_{\text{SECL}} = -\frac{1}{2N} \sum_{i=1}^N \left[\log \frac{\exp(\text{sim}(e(x_i), z_i^{(q)})/\tau)}{\sum_{j \in \mathcal{M}} \exp(\text{sim}(e(x_j), z_i^{(q)})/\tau)} + \log \frac{\exp(\text{sim}(e(x_i), g(s_i))/\tau)}{\sum_{j \in \mathcal{M}} \exp(\text{sim}(e(x_j), g(s_i))/\tau)} \right] \quad (4)$$

Finally, the combined training objective is the sum of two objectives where λ is a hyperparameter to control the contribution of SECL:

$$\mathcal{L} = \mathcal{L}_{\text{INCL}} + \lambda \mathcal{L}_{\text{SECL}} \quad (5)$$

3.3. Transfer Learning

To assess the performance of the pre-trained GAIR, we employ it both as a feature extractor and as an initialization for model fine-tuning. GAIR comprises three encoders: two image encoders dedicated to remote sensing and street view images, and a location encoder responsible for geolocation data representation.

Fine-Tuning the Image Encoders. For Vision Transformers (ViTs), we remove the projection layer and introduce a new head $h(\cdot)$ to process the extracted image feature vectors. Street View Imagery Tasks: $h(\cdot)$ consists of a single linear layer for linear probing and two linear layers for non-linear probing. Remote Sensing Tasks: For semantic segmentation, we use UPerNet [75], while for change detection, we adopt a Siamese UPerNet to capture temporal changes. For multi-temporal dataset, we experiment with two temporal aggregation strategies: (1) a naïve linear mapping, and (2) a lightweight spatial-temporal encoder (L-TAE) [22] to better integrate temporal information.

Fine-Tuning the Location Encoder. We also introduce a new head $h_e(\cdot)$ for the location encoder $e(\cdot)$. Following standard protocols for the geo-aware image classification [42, 74], given a location-image pair (x, I) , where I denotes an image, the model predicts the category y by factorizing the probability as $P(y|I, x) \propto P(y|I)P(y|x)$. Here, $P(y|I)$ is estimated using an image encoder, in this paper, we utilize Inception V3 network [65] following the standard implementation [44, 74], while $e(x)$ contributes to $P(y|x)$. The location encoder is fine-tuned using cross-entropy loss for the geo-aware image classification tasks. For geo-aware image regression tasks, we concatenate the image embedding and location embedding and feed the result into a linear layer for regression. We also use MSE as the loss function.

4. Experiments

Pretraining. We construct a large-scale global distributed per-training dataset **Streetscapes1M** which consists of 1 million triples of (r_i^t, s_i, x_i) . To construct the pre-training dataset, we uniformly sampled 1 million street view images from the Global Streetscapes dataset [29]. To collect the corresponding satellite data, we use the bounding box of each street view image cluster and download the Sentinel-2 remote sensing imagery from Google Earth Engine (GEE). For each bounding box, we download all available RS images using GEE. More specifically, we get all the RS images of the past at a rate of one image per month to form temporal augmentations for RS images. The Sentinel-2 channel consists of 12 surface reflectance multispectral bands with the cirrus band removal. The street view images are with a size of 400×400 and remote sensing data is cropped to a size of 120×120 . We perform all pertaining, fine-tuning, and ablation experiments on a Linux server with 4 NVIDIA

RTXA6000. The ViT we utilize is ViT-b. Please refer to Appendix B.1 and B.5 for the pre-training dataset construction and the implementation details.

Model Fine-Tuning. For street view imagery tasks, we adopt three fine-tuning strategies: *Linear probing*, where the encoder remains frozen, and only a single-layer MLP head is trained; *Non-linear probing*, where the encoder is fixed, and a two-layer MLP head with a sigmoid activation function is optimized; and *Full fine-tuning*, where all model parameters are updated. For remote sensing benchmarks, we fine-tune only the UPerNet while keeping the pretrained backbone frozen. For location-based tasks, we apply full fine-tuning to optimize all parameters. A comprehensive overview of the fine-tuning pipeline, baselines and task configurations is provided in Figure 3 and Appendix B.5.

Benchmarks. To comprehensively evaluate our GAIR, we conduct experiments on 10 different geospatial tasks and 23 datasets. These tasks include 4 street view image tasks – (1) Human perception regression, (2) Socio-economic indicator regression, (3) View direction classification, and (4) Imaging platform classification, 4 remote sensing tasks – (1) Burn scars segmentation, (2) Crop Type Mapping-South Sudan, and (3) Cropland polygon segmentation. 3 geolocation tasks – (1) Species recognition, (2) Remote sensing image regression, and (3) Flickr image classification. Please refer to Figure 3 and Appendix B.3 to detailed descriptions of different tasks and datasets.

Baselines. To thoroughly evaluate the performance of GAIR, we select different sets of baselines for each benchmark category, ensuring a fair and comprehensive comparison.

For street view imagery benchmarks, we compare GAIR against three representative and reproducible GeoFMs: SatMAE [15], CROMA [20], and PIS [1]. These models are strong baselines for geospatial self-supervised learning. Additionally, we include vision models pretrained on large-scale datasets, including a ViT model with randomly initialized weights (Random Init.), a ViT model supervised pretrained on ImageNet (ImageNet Init.) [16, 73], a ViT model pretrained on ImageNet using MoCo-v3 (MoCo v3-ImageNet Init.) [12], and a ViT model pretrained on ImageNet using a MAE-based objective (MAE-ImageNet Init.) [27]. To further validate the effectiveness of GAIR, we introduce self-supervised ViTs trained on our Streetscapes1M dataset, including MoCo v3-Streetscapes and MAE-Streetscapes, which allow us to analyze the benefits of domain-adapted pretraining.

For remote sensing imagery benchmarks, we adopt PANGAEA-Bench [51], a standardized evaluation pipeline that includes 12 GeoFM baselines, please refer to [51] for details about baseline settings. For location benchmarks, we employ LocBench from TorchSpatial [74] to evaluate

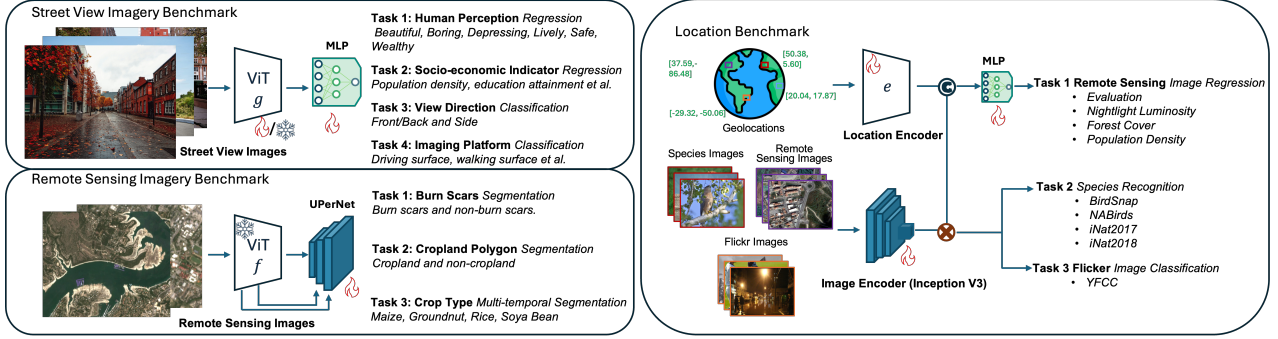


Figure 3. The model evaluation pipelines on three benchmarks covering 10 tasks. Specifically, after pretraining GAIR, we fine-tune the street view image encoder g to tackle the street view imagery benchmark, the RS image encoder f for remote sensing imagery benchmark, and the location encoder e for location benchmark.

the effectiveness of different initialization strategies for RFF. We compare three initialization methods: (1) Random Init., where the model is trained from scratch without any pre-training, (2) GeoCLIP Init., which leverages a pretrained checkpoint from GeoCLIP [69], and (3) GAIR Init., initialized by our pretrained checkpoint. Additionally, we include a No Prior baseline, which solely relies on image features without incorporating location embeddings.

Ablation Study. We conduct ablation studies to analyze the impact of different components in GAIR, including two variants:

- **GAIR-MAE** – In this setting, we replace GAIR’s contrastive learning objective with a masked autoencoder (MAE) pretraining strategy [27]. Specifically, the street view image is treated as a masked region of the remote sensing image, allowing the model to reconstruct missing image patches. A detailed illustration of this approach is provided in Appendix B.3
- **GAIR w/o Loc** – To assess the significance of geolocation encoding, we remove the location embedding $e(x_i)$ from GAIR.

4.1. Street View Imagery Results

Socio-economic Indicator Regression. This task aims at predicting socio-economic indicators from street view images, a widely studied problem in urban analytics [19]. We evaluate models on 10 socio-economic indicators: population density, educational attainment, health condition rates, racial demographics, median household income, proximity to public transportation, percentage of people who walk or bike, proportion of the population over 65 years old, crime rates, and visible sky area, and report RMSE across different fine-tuning settings in Table 1. GAIR achieves the lowest RMSE in the Non-Linear Probing and Fine-Tune All settings, outperforming all baselines. On average, it demonstrates a 10% improvement over other models.

Human Perception Regression. This task assesses human perceptions of urban environments, which are widely used

in urban planning, psychology, and social studies [72]. We perform regression on six perceptual attributes: ‘Beautiful’, ‘Boring’, ‘Depressing’, ‘Lively’, ‘Safe’, and ‘Wealthy’. As shown in Table 1, we can see that GAIR achieves competitive performance, matching or exceeding baseline methods. Notably, the explicit integration of geolocation into contrastive learning significantly enhances model performance, as seen in the substantial improvement from GAIR w/o Loc to GAIR.

View Direction Classification. View direction reflects the model’s ability to capture geospatial context. This task involves classifying images into two categories: “front/back” and “side”. As shown in Table 1, existing Geo-Foundation Models struggle with view direction estimation, whereas GAIR consistently outperforms all baselines, demonstrating its superior spatial awareness.

Imaging Platform Classification. Different imaging platforms offer distinct perspectives on the built and natural environment. For this task we include 6 platform types, including driving surface, walking surface, cycling surface, tuner, open fields, and railway. As shown in Table 1, GAIR outperforms all baselines on all settings.

4.2. Remote Sensing Results

Table 2 presents the evaluation results of GAIR across three remote sensing tasks.

Single Temporal Semantic Segmentation We evaluate GAIR on two single-temporal segmentation tasks: burn scar segmentation using the HLS Burns dataset [34] and cropland polygon delineation using the AI4SmallFarms dataset [56], both based on Sentinel-2 imagery. GAIR achieves a mean Intersection over Union (mIoU) of 83.26% for burn scars and 43.35% for cropland segmentation, outperforming all baselines. Notably, GAIR improves performance by 0.5% for burn scars and 16.16% for cropland segmentation, demonstrating its capability in extracting meaningful geospatial features for land cover classification.

Table 1. Comparisons of model performance across street view imagery benchmark. RMSE ↓ is reported for *socio-economic indicator regression and human perception regression*, while F1 score ↑ is reported for *view direction classification and imaging platform classification*. The best and second best results are denoted as **Bold** and Underline.

Model	Socio-Economic Indicator (RMSE ↓)			Human Perception (RMSE ↓)			View Direction (F1 ↑)			Imaging Platform (F1 ↑)		
	Linear	Non-Linear	All	Linear	Non-Linear	All	Linear	Non-Linear	All	Linear	Non-Linear	All
SatMAE[15]	0.9671	0.9421	0.7690	2.1681	2.1196	1.8812	0.0000	0.0202	0.3885	0.1916	0.1596	0.2114
Croma[20]	0.9550	0.9295	0.7927	2.0768	2.0219	1.9387	0.0064	0.0640	0.2133	0.1733	0.1832	0.2369
PIS[1]	0.9290	0.8911	0.6797	1.9858	1.8865	1.6166	0.1937	0.2442	0.3537	0.2315	0.2796	0.3328
Random Init.	0.9700	0.9524	0.9035	2.2000	2.1534	2.1839	0.0000	0.0000	0.3954	0.1834	0.1895	0.1970
ImageNet Init.[16, 73]	0.8929	0.8489	0.7012	<u>1.7473</u>	1.6439	<u>1.5271</u>	<u>0.5328</u>	0.4186	0.5850	0.3229	0.3275	0.3540
MoCo v3-ImageNet[12]	0.8760	0.8441	0.6779	1.7590	1.6599	1.5821	0.2106	0.6262	0.4976	0.2584	0.3171	0.3161
MAE-ImageNet[27]	0.8816	0.8373	0.7150	1.8730	1.7592	1.5788	0.4298	<u>0.6426</u>	0.4961	0.2619	0.3257	0.2195
MoCo v3-Streetscapes	0.8863	0.8429	<u>0.6707</u>	1.7601	1.7084	1.5800	0.3508	0.5988	0.5032	0.3439	0.3308	0.3639
MAE-Streetscapes	0.8940	0.8416	0.6872	1.8514	1.7701	1.5774	0.3451	0.6102	0.4921	0.3335	0.3482	0.3050
GAIR-MAE	0.9485	0.9011	0.8048	2.1254	2.0495	1.9611	0.0272	0.0895	0.3029	0.2124	0.2582	0.3249
GAIR w/o Loc	0.8823	<u>0.8352</u>	0.6725	<u>1.7473</u>	1.6782	1.5960	0.5290	0.6052	<u>0.6078</u>	<u>0.3676</u>	<u>0.3709</u>	<u>0.3892</u>
GAIR	<u>0.8803</u>	0.8349	0.6612	1.7141	<u>1.6489</u>	1.5072	0.5457	0.6495	0.6102	0.3793	0.3782	0.4071

Table 2. Performance comparison (mIoU ↑) of GAIR and other Geo-Foundation Models (GeoFMs) across four remote sensing benchmark datasets. SS refers to semantic segmentation tasks, while Linear and L-TAE [22] represent two different multi-temporal augmentation strategies

Task	Single Temporal SS		Multi Temporal SS	
	Burn Scars	Cropland Polygon	Crop Type	
			Linear	L-TAE
Model				
CROMA [20]	81.95	25.65	47.02	49.38
DOFA [76]	78.96	27.07	49.81	51.33
GFM-Swin [52]	76.17	27.19	39.72	46.98
Prithvi [34]	82.67	26.86	39.92	43.07
RemoteCLIP [39]	75.55	25.12	46.50	52.05
SatlasNet [6]	79.69	25.13	46.97	46.97
Scale-MAE [58]	76.71	21.47	21.39	25.42
SpectralGPT [28]	80.47	26.75	53.50	46.95
S12-Data2Vec [61]	81.14	24.23	54.01	<u>54.03</u>
S12-DINO [61]	81.44	25.62	46.56	48.66
S12-MAE [61]	80.86	24.69	46.28	45.80
S12-MoCo [61]	80.76	25.38	44.22	48.58
GAIR-MAE	74.15	22.77	34.18	40.44
GAIR w/o Loc	<u>82.94</u>	<u>43.28</u>	<u>55.41</u>	54.32
GAIR	83.26	43.35	55.53	54.01

Multi Temporal Semantic Segmentation For this task, we utilize the Crop Type Mapping dataset [41], which consists of Sentinel-2 imagery from 2017. To utilize temporal information, we employ two widely used feature aggregation strategies: linear aggregation and L-TAE aggregation. GAIR consistently outperforms other baselines, particularly in the simpler linear aggregation setting, achieving a 1% mIoU improvement.

4.3. Location Benchmark Results

Here, we evaluate 3 location tasks, Table 3 shows all the results.

Geo-Aware Image Regression. We evaluate the effectiveness of location priors using the MOSAIKS dataset [59], which includes four regression tasks: population density, forest cover, nightlight luminosity, and elevation estimation. The results indicate that incorporating location information

significantly enhances model performance, yielding up to a 50% improvement over models without location priors. Furthermore, using pretrained checkpoints further refines the learned geospatial representations. In particular, pretraining with GAIR provides the greatest gains, achieving improvements of 0.06, 0.02, 0.03, and 0.04 in R^2 for population density, forest cover, nightlight luminosity, and elevation regression, respectively.

Geo-Aware Species Recognition. This task aims to classify images of different animal species. We use four datasets: BirdSnap [7], NABirds [67], iNat2017 [68], and iNat2018 [68]. Using a pretrained GeoCLIP encoder provides a moderate performance boost over random initialization. Notably, GAIR achieves the best results, consistently outperforming other baselines by improving the Top-1 accuracy by up to 1.5% on BirdSnap and NABirds, and around 0.5% on the larger-scale iNat datasets. These improvements suggest that GAIR’s location-aware encoding effectively captures spatial patterns associated with species distribution.

Geo-Aware Flickr Image Classification. We adopt the YFCC100M-GEO100 dataset (YFCC) [77], which contains 100 everyday object categories with geolocation annotations. From the results, we observe that the *No Prior* baseline, which excludes geolocation features, yields the lowest performance. This suggests location information is a valuable cue for image classification. However, the impact of model initialization remains minimal, which is due to the dataset’s large scale and the relatively small capacity of the location encoder, which limits the pretraining benefits.

5. Discussions

5.1. Multi-modal Pretraining Effectiveness

GAIR explicitly incorporates location information to fuse street view and remote sensing data, demonstrating significant performance improvements in single-modal tasks when pre-trained with geo-aligned multi-modal contrastive objectives. Our results indicate that using both modalities during

Table 3. Evaluation results on LocBench [74], including three tasks: image regression (4 datasets), species recognition (4 datasets), and Flickr image classification (1 dataset). For image regression tasks, we report the R^2 score (\uparrow), while for species recognition and Flickr classification, we report the Top-1 accuracy (\uparrow).

Initialization	Task	Image Regression				
	Model	Population Density	Forest Cover	Nightlight Luminosity	Elevation	
Random Init.	No Prior	0.38	0.52	0.33	0.27	
	RFF	0.57	0.84	0.35	0.76	
GeoCLIP Init.	RFF	0.61	0.84	0.37	0.78	
GAIR Init.	RFF	0.67	0.86	0.40	0.82	
Initialization	Task	Species Recognition				Flicker Classification
	Model	BirdSnap	NABirds	iNat2017	iNat2018	YFCC
Random Init.	No Prior	70.07	76.08	63.27	60.20	50.15
	RFF	70.07	81.63	67.73	71.66	51.13
GeoCLIP Init.	RFF	70.56	81.65	67.78	71.93	51.01
GAIR Init.	RFF	72.07	81.76	67.84	72.48	51.13

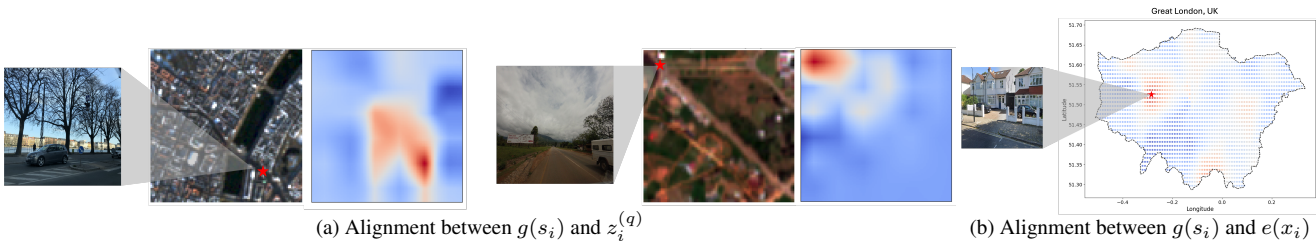


Figure 4. Visualization of spatial alignment across different modalities in GAIR using heat maps. The red star indicates the geographic location of the street view (SV) image s_i . (a) Cosine similarity between the SV image embedding $g(s_i)$ and the localized remote sensing (RS) image embeddings $\hat{r}_i(x)$. (b) Cosine similarity between $g(s_i)$ and the location embeddings $e(x_i)$. Spatial grids are uniformly sampled across the Greater London region to generate location embeddings. More visualizations can be seen in Appendix B.8

pretraining enhances accuracy compared to training with only a single modality (e.g., either street view or remote sensing data). As shown in Tables 1, GAIR consistently surpasses MoCo v3 and MAE trained solely on Streetscapes1M, achieving up to a 0.1 reduction in RMSE and a 0.2 increase in F1 score. Additionally, our ablation study highlights the critical role of Spatially Explicit Contrastive Learning (SECL) in effectively aligning geospatial features across modalities. Notably, despite the fact that Streetscapes1M primarily focuses on street view images with limited remote sensing diversity, GAIR still shows competitive performance in remote sensing benchmarks. Even with significantly fewer remote sensing patches compared to other GeoFMs (only 0.1 million remote sensing samples, as illustrated in Appendix B.6), GAIR outperforms GeoFMs trained on large-scale remote sensing datasets, as evidenced in Table 2. This suggests that integrating street view imagery and location information effectively compensates for the relatively smaller volume of remote sensing data.

5.2. Qualitative Analysis of Geo-Alignment across Data Modalities

To assess whether GAIR effectively captures spatial relationships across different data modalities, we first compute the cosine similarities between a given street view image embedding $g(s_i) \in \mathbb{R}^D$ and different localized remote sensing image embedding $z_i^{(q)}$ generated by Ω at different location

$x_i^{(q)}$. As illustrated in Figure 4(a), GAIR successfully learns to geographically align these two representations. Furthermore, to analyze the similarities between a given street view image embedding $g(s_i) \in \mathbb{R}^D$ and location embeddings at different locations, we use the known geolocation x_i of the street view image s_i as a reference point, generate a uniform mesh grid surround x_i with a spatial resolution of 0.01° . Our pretrained location encoder $e(\cdot)$ of GAIR can produce a set of location embeddings of all these mesh grid locations. We compute the cosine similarity between the street view image embedding $g(s_i)$ and these location embeddings. As shown in Figure 4(b), GAIR successfully aligns location-based representations with street-level image features.

6. Conclusion

We introduce GAIR, a new GeoFM that integrates remote sensing imagery, street view imagery, and geolocation data to enhance geospatial representation learning. Unlike existing GeoFMs that primarily focus on single-modal remote sensing data, GAIR explicitly models cross-scale spatial relationships by leveraging Implicit Neural Representations (INR) and Spatially Explicit Contrastive Learning (SECL). These techniques enable the alignment of overhead and ground-level imagery while preserving geospatial proximity in the learned embeddings. Extensive experiments have been conducted across 10 geospatial tasks, and GAIR consistently outperforms SOTA baselines in all settings.

References

- [1] Xiao An, Wei He, Jiaqi Zou, Guangyi Yang, and Hongyan Zhang. Pretrain a remote sensing foundation model by promoting intra-instance similarity. *IEEE Transactions on Geoscience and Remote Sensing*, 2024. 5, 7, 13
- [2] Guillaume Astruc, Nicolas Gonthier, Clement Mallet, and Loic Landrieu. Omnisat: Self-supervised modality fusion for earth observation. In *European Conference on Computer Vision*, pages 409–427. Springer, 2024. 2, 16
- [3] Guillaume Astruc, Nicolas Gonthier, Clement Mallet, and Loic Landrieu. Omnisat: Self-supervised modality fusion for earth observation. In *European Conference on Computer Vision*, pages 409–427. Springer, 2025. 2
- [4] Kumar Ayush, Burak Uzket, Chenlin Meng, Kumar Tanmay, Marshall Burke, David Lobell, and Stefano Ermon. Geography-aware self-supervised learning. In *Proceedings of the IEEE/CVF International Conference on Computer Vision*, pages 10181–10190, 2021. 2
- [5] George Azzari, Meha Jain, and David B Lobell. Towards fine resolution global maps of crop yields: Testing multiple methods and satellites in three countries. *Remote Sensing of Environment*, 202:129–141, 2017. 1
- [6] Favyen Bastani, Piper Wolters, Ritwik Gupta, Joe Ferdinando, and Aniruddha Kembhavi. Satlaspretrain: A large-scale dataset for remote sensing image understanding. In *Proceedings of the IEEE/CVF International Conference on Computer Vision*, pages 16772–16782, 2023. 7
- [7] Thomas Berg, Jiongxin Liu, Seung Woo Lee, Michelle L Alexander, David W Jacobs, and Peter N Belhumeur. Birdsnap: Large-scale fine-grained visual categorization of birds. In *Proceedings of the IEEE conference on computer vision and pattern recognition*, pages 2011–2018, 2014. 7, 15
- [8] Ling Cai, Krzysztof Janowicz, Gengchen Mai, Bo Yan, and Rui Zhu. Traffic transformer: Capturing the continuity and periodicity of time series for traffic forecasting. *Transactions in GIS*, 24(3):736–755, 2020. 1
- [9] Jiezhong Cao, Qin Wang, Yongqin Xian, Yawei Li, Bingbing Ni, Zhiming Pi, Kai Zhang, Yulun Zhang, Radu Timofte, and Luc Van Gool. Ciaosr: Continuous implicit attention-inattention network for arbitrary-scale image super-resolution. In *Proceedings of the IEEE/CVF Conference on Computer Vision and Pattern Recognition*, pages 1796–1807, 2023. 3
- [10] Mathilde Caron, Hugo Touvron, Ishan Misra, Hervé Jégou, Julien Mairal, Piotr Bojanowski, and Armand Joulin. Emerging properties in self-supervised vision transformers. In *Proceedings of the IEEE/CVF international conference on computer vision*, pages 9650–9660, 2021. 2
- [11] Ting Chen, Simon Kornblith, Mohammad Norouzi, and Geoffrey Hinton. A simple framework for contrastive learning of visual representations. In *International conference on machine learning*, pages 1597–1607. PMLR, 2020.
- [12] Xinlei Chen*, Saining Xie*, and Kaiming He. An empirical study of training self-supervised vision transformers. *arXiv preprint arXiv:2104.02057*, 2021. 2, 5, 7
- [13] Yinbo Chen, Sifei Liu, and Xiaolong Wang. Learning continuous image representation with local implicit image function. In *Proceedings of the IEEE/CVF conference on computer vision and pattern recognition*, pages 8628–8638, 2021. 2, 3, 13
- [14] Elijah Cole, Grant Van Horn, Christian Lange, Alexander Shepard, Patrick Leary, Pietro Perona, Scott Loarie, and Oisín Mac Aodha. Spatial implicit neural representations for global-scale species mapping. In *International Conference on Machine Learning*, pages 6320–6342. PMLR, 2023. 1, 3
- [15] Yezhen Cong, Samar Khanna, Chenlin Meng, Patrick Liu, Erik Rozi, Yutong He, Marshall Burke, David Lobell, and Stefano Ermon. Satmae: Pre-training transformers for temporal and multi-spectral satellite imagery. *Advances in Neural Information Processing Systems*, 35:197–211, 2022. 1, 2, 5, 7, 13, 16
- [16] Jia Deng, Wei Dong, Richard Socher, Li-Jia Li, Kai Li, and Li Fei-Fei. Imagenet: A large-scale hierarchical image database. In *2009 IEEE conference on computer vision and pattern recognition*, pages 248–255. Ieee, 2009. 2, 5, 7
- [17] Alexey Dosovitskiy. An image is worth 16x16 words: Transformers for image recognition at scale. *arXiv preprint arXiv:2010.11929*, 2020. 3
- [18] Emilien Dupont, Adam Goliński, Milad Alizadeh, Yee Whye Teh, and Arnaud Doucet. Coin: Compression with implicit neural representations. *arXiv preprint arXiv:2103.03123*, 2021. 3
- [19] Zhuangyuan Fan, Fan Zhang, Becky PY Loo, and Carlo Ratti. Urban visual intelligence: Uncovering hidden city profiles with street view images. *Proceedings of the National Academy of Sciences*, 120(27):e2220417120, 2023. 6
- [20] Anthony Fuller, Koreen Millard, and James Green. Croma: Remote sensing representations with contrastive radar-optical masked autoencoders. *Advances in Neural Information Processing Systems*, 36, 2024. 2, 5, 7, 13, 16
- [21] Sicheng Gao, Xuhui Liu, Bohan Zeng, Sheng Xu, Yanjing Li, Xiaoyan Luo, Jianzhuang Liu, Xiantong Zhen, and Baochang Zhang. Implicit diffusion models for continuous super-resolution. In *Proceedings of the IEEE/CVF conference on computer vision and pattern recognition*, pages 10021–10030, 2023. 2, 3
- [22] Vivien Sainte Fare Garnot and Loic Landrieu. Lightweight temporal self-attention for classifying satellite images time series. In *Advanced Analytics and Learning on Temporal Data: 5th ECML PKDD Workshop, AALTD 2020, Ghent, Belgium, September 18, 2020, Revised Selected Papers 6*, pages 171–181. Springer, 2020. 5, 7
- [23] Jean-Bastien Grill, Florian Strub, Florent Altché, Corentin Tallec, Pierre Richemond, Elena Buchatskaya, Carl Doersch, Bernardo Avila Pires, Zhaohan Guo, Mohammad Gheshlaghi Azar, et al. Bootstrap your own latent—a new approach to self-supervised learning. *Advances in neural information processing systems*, 33:21271–21284, 2020. 2
- [24] Xin Guo, Jiangwei Lao, Bo Dang, Yingying Zhang, Lei Yu, Lixiang Ru, Liheng Zhong, Ziyuan Huang, Kang Wu, Dingxiang Hu, et al. Skysense: A multi-modal remote sensing

- foundation model towards universal interpretation for earth observation imagery. In *Proceedings of the IEEE/CVF Conference on Computer Vision and Pattern Recognition*, pages 27672–27683, 2024. 2, 3
- [25] Yoo-Geun Ham, Jeong-Hwan Kim, and Jing-Jia Luo. Deep learning for multi-year ENSO forecasts. *Nature*, 573(7775): 568–572, 2019. 1
- [26] Kaiming He, Haoqi Fan, Yuxin Wu, Saining Xie, and Ross Girshick. Momentum contrast for unsupervised visual representation learning. In *Proceedings of the IEEE/CVF conference on computer vision and pattern recognition*, pages 9729–9738, 2020. 2, 4
- [27] Kaiming He, Xinlei Chen, Saining Xie, Yanghao Li, Piotr Dollár, and Ross Girshick. Masked autoencoders are scalable vision learners. In *Proceedings of the IEEE/CVF conference on computer vision and pattern recognition*, pages 16000–16009, 2022. 2, 5, 6, 7, 13
- [28] Danfeng Hong, Bing Zhang, Xuyang Li, Yuxuan Li, Chenyu Li, Jing Yao, Naoto Yokoya, Hao Li, Pedram Ghamisi, Xiuping Jia, et al. Spectralgpt: Spectral remote sensing foundation model. *IEEE Transactions on Pattern Analysis and Machine Intelligence*, 2024. 2, 7, 16
- [29] Yujun Hou, Matias Quintana, Maxim Khomiakov, Winston Yap, Jiani Ouyang, Koichi Ito, Zeyu Wang, Tianhong Zhao, and Filip Biljecki. Global streetscapes—a comprehensive dataset of 10 million street-level images across 688 cities for urban science and analytics. *ISPRS Journal of Photogrammetry and Remote Sensing*, 215:216–238, 2024. 5, 13, 14
- [30] Chia-Yu Hsu, Wenwen Li, and Sizhe Wang. Geospatial foundation models for image analysis: Evaluating and enhancing nasa-ibm prithvi’s domain adaptability. *International Journal of Geographical Information Science*, pages 1–30, 2024. 2
- [31] Max Jaderberg, Karen Simonyan, Andrew Zisserman, et al. Spatial transformer networks. *Advances in neural information processing systems*, 28, 2015. 3
- [32] Pallavi Jain, Dino Ienco, Roberto Interdonato, Tristan Berchoux, and Diego Marcos. Senclip: Enhancing zero-shot land-use mapping for sentinel-2 with ground-level prompting. *arXiv preprint arXiv:2412.08536*, 2024. 16
- [33] Umangi Jain, Alex Wilson, and Varun Gulshan. Multimodal contrastive learning for remote sensing tasks. *arXiv preprint arXiv:2209.02329*, 2022. 2
- [34] Johannes Jakubik, Sujit Roy, CE Phillips, Paolo Fraccaro, Denys Godwin, Bianca Zadrozny, Daniela Szwarcman, Carlos Gomes, Gabby Nyirjesy, Blair Edwards, et al. Foundation models for generalist geospatial artificial intelligence. *arXiv preprint arXiv:2310.18660*, 2023. 6, 7, 14
- [35] Neal Jean, Marshall Burke, Michael Xie, W Matthew Davis, David B Lobell, and Stefano Ermon. Combining satellite imagery and machine learning to predict poverty. *Science*, 353(6301):790–794, 2016. 1
- [36] Konstantin Klemmer, Esther Rolf, Caleb Robinson, Lester Mackey, and Marc Rußwurm. Satclip: Global, general-purpose location embeddings with satellite imagery. *arXiv preprint arXiv:2311.17179*, 2023. 1, 2, 3
- [37] Hao Li, Benjamin Herfort, Sven Lautenbach, Jiaoyan Chen, and Alexander Zipf. Improving openstreetmap missing building detection using few-shot transfer learning in sub-saharan africa. *Transactions in GIS*, 26(8):3125–3146, 2022. 1
- [38] Hao Li, Jiapan Wang, Johann Maximilian Zollner, Gengchen Mai, Ni Lao, and Martin Werner. Rethink geographical generalizability with unsupervised self-attention model ensemble: A case study of openstreetmap missing building detection in africa. In *Proceedings of the 31st ACM International Conference on Advances in Geographic Information Systems*, pages 1–9, 2023. 1
- [39] Fan Liu, Delong Chen, Zhangqingyun Guan, Xiaocong Zhou, Jiale Zhu, Qiaolin Ye, Liyong Fu, and Jun Zhou. Remoteclip: A vision language foundation model for remote sensing. *IEEE Transactions on Geoscience and Remote Sensing*, 2024. 7
- [40] Ze Liu, Yutong Lin, Yue Cao, Han Hu, Yixuan Wei, Zheng Zhang, Stephen Lin, and Baining Guo. Swin transformer: Hierarchical vision transformer using shifted windows. In *Proceedings of the IEEE/CVF international conference on computer vision*, pages 10012–10022, 2021. 2
- [41] Rose M Rustowicz, Robin Cheong, Lijing Wang, Stefano Ermon, Marshall Burke, and David Lobell. Semantic segmentation of crop type in africa: A novel dataset and analysis of deep learning methods. In *Proceedings of the IEEE/cvf conference on computer vision and pattern recognition workshops*, pages 75–82, 2019. 7, 14
- [42] Oisín Mac Aodha, Elijah Cole, and Pietro Perona. Presence-only geographical priors for fine-grained image classification. In *Proceedings of the IEEE/CVF International Conference on Computer Vision*, pages 9596–9606, 2019. 3, 5, 15
- [43] Gengchen Mai, Krzysztof Janowicz, Ling Cai, Rui Zhu, Blake Regalia, Bo Yan, Meilin Shi, and Ni Lao. Se-kge: A location-aware knowledge graph embedding model for geographic question answering and spatial semantic lifting. *Transactions in GIS*, 24(3):623–655, 2020. 1, 3
- [44] Gengchen Mai, Krzysztof Janowicz, Bo Yan, Rui Zhu, Ling Cai, and Ni Lao. Multi-scale representation learning for spatial feature distributions using grid cells. In *International Conference on Learning Representations*, 2020. 3, 5
- [45] Gengchen Mai, Krzysztof Janowicz, Bo Yan, Rui Zhu, Ling Cai, and Ni Lao. Multi-scale representation learning for spatial feature distributions using grid cells. *arXiv preprint arXiv:2003.00824*, 2020. 2
- [46] Gengchen Mai, Ni Lao, Yutong He, Jiaming Song, and Stefano Ermon. Csp: Self-supervised contrastive spatial pre-training for geospatial-visual representations. In *International Conference on Machine Learning*, pages 23498–23515. PMLR, 2023. 1, 2, 3
- [47] Gengchen Mai, Yao Xuan, Wenyun Zuo, Yutong He, Jiaming Song, Stefano Ermon, Krzysztof Janowicz, and Ni Lao. Sphere2vec: A general-purpose location representation learning over a spherical surface for large-scale geospatial predictions. *ISPRS Journal of Photogrammetry and Remote Sensing*, 202:439–462, 2023. 1, 3
- [48] Gengchen Mai, Weiming Huang, Jin Sun, Suhang Song, Deepak Mishra, Ninghao Liu, Song Gao, Tianming Liu, Gao Cong, Yingjie Hu, et al. On the opportunities and challenges of foundation models for geospatial (vision paper). *ACM Transactions on Spatial Algorithms and Systems*, 2024. 2

- [49] Gengchen Mai, Yiqun Xie, Xiaowei Jia, Ni Lao, Jinneng Rao, Qing Zhu, Zeping Liu, Yao-Yi Chiang, and Junfeng Jiao. Towards the next generation of geospatial artificial intelligence. *International Journal of Applied Earth Observation and Geoinformation*, 136:104368, 2025. 1
- [50] Oscar Manas, Alexandre Lacoste, Xavier Giró-i Nieto, David Vazquez, and Pau Rodriguez. Seasonal contrast: Unsupervised pre-training from uncurated remote sensing data. In *Proceedings of the IEEE/CVF International Conference on Computer Vision*, pages 9414–9423, 2021. 2
- [51] Valerio Marsocci, Yuru Jia, Georges Le Bellier, David Kerekes, Liang Zeng, Sebastian Hafner, Sebastian Gerard, Eric Brune, Ritu Yadav, Ali Shibli, Heng Fang, Yifang Ban, Maarten Vergauwen, Nicolas Audebert, and Andrea Nascetti. Pangaea: A global and inclusive benchmark for geospatial foundation models, 2024. 5, 16
- [52] Matías Mendieta, Boran Han, Xingjian Shi, Yi Zhu, Chen Chen, and Mu Li. Gfm: Building geospatial foundation models via continual pretraining. *arXiv preprint arXiv:2302.04476*, 3, 2023. 7
- [53] Lars Mescheder, Michael Oechsle, Michael Niemeyer, Sebastian Nowozin, and Andreas Geiger. Occupancy networks: Learning 3d reconstruction in function space. In *Proceedings of the IEEE/CVF Conference on Computer Vision and Pattern Recognition*, pages 4460–4470, 2019. 3
- [54] Tung Nguyen, Johannes Brandstetter, Ashish Kapoor, Jayesh K Gupta, and Aditya Grover. Climax: A foundation model for weather and climate. *arXiv preprint arXiv:2301.10343*, 2023. 2
- [55] Maxime Oquab, Timothée Darcet, Théo Moutakanni, Huy Vo, Marc Szafraniec, Vasil Khalidov, Pierre Fernandez, Daniel Haziza, Francisco Massa, Alaaeldin El-Nouby, et al. Dinov2: Learning robust visual features without supervision. *arXiv preprint arXiv:2304.07193*, 2023. 2
- [56] Claudio Persello, Jeroen Grift, Xinyan Fan, Claudia Paris, Ronny Hänsch, Mila Koeva, and Andrew Nelson. Ai4smallfarms: A dataset for crop field delineation in south-east asian smallholder farms. *IEEE Geoscience and Remote Sensing Letters*, 20:1–5, 2023. 6, 14
- [57] Alec Radford, Jong Wook Kim, Chris Hallacy, Aditya Ramesh, Gabriel Goh, Sandhini Agarwal, Girish Sastry, Amanda Askell, Pamela Mishkin, Jack Clark, et al. Learning transferable visual models from natural language supervision. In *International conference on machine learning*, pages 8748–8763. PMLR, 2021. 2, 3, 4
- [58] Colorado J Reed, Ritwik Gupta, Shufan Li, Sarah Brockman, Christopher Funk, Brian Clipp, Kurt Keutzer, Salvatore Candido, Matt Uyttendaele, and Trevor Darrell. Scale-mae: A scale-aware masked autoencoder for multiscale geospatial representation learning. In *Proceedings of the IEEE/CVF International Conference on Computer Vision*, pages 4088–4099, 2023. 7
- [59] Esther Rolf, Jonathan Proctor, Tamma Carleton, Ian Bolliger, Vaishaal Shankar, Miyabi Ishihara, Benjamin Recht, and Solomon Hsiang. A generalizable and accessible approach to machine learning with global satellite imagery. *Nature communications*, 12(1):4392, 2021. 7, 14
- [60] Vincent Sitzmann, Julien Martel, Alexander Bergman, David Lindell, and Gordon Wetzstein. Implicit neural representations with periodic activation functions. *Advances in neural information processing systems*, 33:7462–7473, 2020. 2
- [61] Adam Stewart, Nils Lehmann, Isaac Corley, Yi Wang, Yi-Chia Chang, Nassim Ait Ali Braham, Shradha Sehgal, Caleb Robinson, and Arindam Banerjee. Ssl4eo-1: Datasets and foundation models for landsat imagery. *Advances in Neural Information Processing Systems*, 36:59787–59807, 2023. 7
- [62] Vldan Stojnic and Vladimir Risojevic. Self-supervised learning of remote sensing scene representations using contrastive multiview coding. In *Proceedings of the IEEE/CVF Conference on Computer Vision and Pattern Recognition*, pages 1182–1191, 2021. 2
- [63] Brian L Sullivan, Christopher L Wood, Marshall J Iliff, Rick E Bonney, Daniel Fink, and Steve Kelling. ebird: A citizen-based bird observation network in the biological sciences. *Biological conservation*, 142(10):2282–2292, 2009. 15
- [64] Xian Sun, Peijin Wang, Wanxuan Lu, Zicong Zhu, Xiaonan Lu, Qibin He, Junxi Li, Xue Rong, Zhujun Yang, Hao Chang, et al. Ringmo: A remote sensing foundation model with masked image modeling. *IEEE Transactions on Geoscience and Remote Sensing*, 61:1–22, 2022. 2
- [65] Christian Szegedy, Vincent Vanhoucke, Sergey Ioffe, Jon Shlens, and Zbigniew Wojna. Rethinking the inception architecture for computer vision. In *Proceedings of the IEEE conference on computer vision and pattern recognition*, pages 2818–2826, 2016. 5
- [66] Matthew Tancik, Pratul Srinivasan, Ben Mildenhall, Sara Fridovich-Keil, Nithin Raghavan, Utkarsh Singhal, Ravi Ramamoorthi, Jonathan Barron, and Ren Ng. Fourier features let networks learn high frequency functions in low dimensional domains. *Advances in Neural Information Processing Systems*, 33:7537–7547, 2020. 3
- [67] Grant Van Horn, Steve Branson, Ryan Farrell, Scott Haber, Jessie Barry, Panos Ipeirotis, Pietro Perona, and Serge Belongie. Building a bird recognition app and large scale dataset with citizen scientists: The fine print in fine-grained dataset collection. In *Proceedings of the IEEE conference on computer vision and pattern recognition*, pages 595–604, 2015. 7, 15
- [68] Grant Van Horn, Oisín Mac Aodha, Yang Song, Yin Cui, Chen Sun, Alex Shepard, Hartwig Adam, Pietro Perona, and Serge Belongie. The inaturalist species classification and detection dataset. In *Proceedings of the IEEE conference on computer vision and pattern recognition*, pages 8769–8778, 2018. 7, 15
- [69] Vicente Vivanco Cepeda, Gaurav Kumar Nayak, and Mubarak Shah. Geoclip: Clip-inspired alignment between locations and images for effective worldwide geo-localization. *Advances in Neural Information Processing Systems*, 36, 2024. 3, 4, 6
- [70] Wenhui Wang, Hangbo Bao, Li Dong, Johan Bjorck, Zhiliang Peng, Qiang Liu, Kriti Aggarwal, Owais Khan Mohammed, Saksham Singhal, Subhojit Som, et al. Image as a foreign language: Beit pretraining for vision and vision-language tasks.

- In *Proceedings of the IEEE/CVF Conference on Computer Vision and Pattern Recognition*, pages 19175–19186, 2023. 2
- [71] Xinye Wanyan, Sachith Seneviratne, Shuchang Shen, and Michael Kirley. Dino-mc: Self-supervised contrastive learning for remote sensing imagery with multi-sized local crops. *arXiv preprint arXiv:2303.06670*, 2023. 2
- [72] Jingxian Wei, Wenze Yue, Mengmeng Li, and Jiabin Gao. Mapping human perception of urban landscape from street-view images: A deep-learning approach. *International Journal of Applied Earth Observation and Geoinformation*, 112: 102886, 2022. 6
- [73] Bichen Wu, Chenfeng Xu, Xiaoliang Dai, Alvin Wan, Peizhao Zhang, Zhicheng Yan, Masayoshi Tomizuka, Joseph Gonzalez, Kurt Keutzer, and Peter Vajda. Visual transformers: Token-based image representation and processing for computer vision, 2020. 5, 7
- [74] Nemin Wu, Qian Cao, Zhangyu Wang, Zeping Liu, Yanlin Qi, Jieli Zhang, Joshua Ni, Xiaobai Yao, Hongxu Ma, Lan Mu, et al. Torchspatial: A location encoding framework and benchmark for spatial representation learning. *arXiv preprint arXiv:2406.15658*, 2024. 1, 2, 3, 5, 8, 16
- [75] Tete Xiao, Yingcheng Liu, Bolei Zhou, Yuning Jiang, and Jian Sun. Unified perceptual parsing for scene understanding. In *Proceedings of the European conference on computer vision (ECCV)*, pages 418–434, 2018. 5
- [76] Zhitong Xiong, Yi Wang, Fahong Zhang, Adam J Stewart, Joëlle Hanna, Damian Borth, Ioannis Papoutsis, Bertrand Le Saux, Gustau Camps-Valls, and Xiao Xiang Zhu. Neural plasticity-inspired foundation model for observing the earth crossing modalities. *arXiv e-prints*, pages arXiv–2403, 2024. 2, 7, 16
- [77] Yahoo. Yahoo flickr creative commons 100m. <http://webscope.sandbox.yahoo.com/catalog.php?datatype=i&did=67>. Accessed: 2024-06-03. 7, 15
- [78] Christopher Yeh, Chenlin Meng, Sherrie Wang, Anne Driscoll, Erik Rozi, Patrick Liu, Jihyeon Lee, Marshall Burke, David B Lobell, and Stefano Ermon. Sustainbench: Benchmarks for monitoring the sustainable development goals with machine learning. *arXiv preprint arXiv:2111.04724*, 2021. 14
- [79] Jiaxuan You, Xiaocheng Li, Melvin Low, David Lobell, and Stefano Ermon. Deep gaussian process for crop yield prediction based on remote sensing data. In *Proceedings of the AAAI conference on artificial intelligence*, 2017. 1
- [80] Dazhou Yu, Riyang Bao, Gengchen Mai, and Liang Zhao. Spatial-rag: Spatial retrieval augmented generation for real-world spatial reasoning questions. *arXiv preprint arXiv:2502.18470*, 2025. 1
- [81] Pengchuan Zhang, Xiujun Li, Xiaowei Hu, Jianwei Yang, Lei Zhang, Lijuan Wang, Yejin Choi, and Jianfeng Gao. Vinvl: Revisiting visual representations in vision-language models. In *Proceedings of the IEEE/CVF conference on computer vision and pattern recognition*, pages 5579–5588, 2021. 2

A. Methods

A.1. Feature Unfolding

Here, for each cell in the $P \times P$ coordinate grid, we concatenate its neighboring features, i.e., 3×3 surrounding patch into a single extended vector and obtain an expanded feature map and obtain a feature map with dimension $P \times P \times 9D$, this process can increase the receptive field of each latent code and equip the INR with information from a local neighborhood when predicting signals.

A.2. Local Ensemble Interpolation

We parameterize the continuous function with a small neural network f_θ (a single layer perceptron). This implicit decoder f_θ is shared across all images and takes two inputs: (a) a latent code (feature vector) z , and (b) a continuous 2D coordinate offset Δx within that latent code’s cell. If we only encode the latent code which nearest to the query location x_i^q could lead to discontinuities at cell boundaries [13]. To ensure smooth transitions across space, we use a local ensemble interpolation strategy. Instead of relying on a single latent code, we query the four latent codes $z_i^{(k)}$ ($k \in \{00, 01, 10, 11\}$) corresponding to the cell corners surrounding the continuous coordinate. Each code produces a prediction $f_\theta(z_i^{(k)}, x_i^{(q)} - x_i^{(k)})$, and we blend these outputs with weights proportional to the area of the cell corner (or equivalently, bilinear interpolation weights based on the coordinate’s fractional position within the cell).

B. Experimental Details

B.1. Streetscape1M Dataset Construction Details

In order to construct a global scale geospatial aligned multimodal dataset for GAIR model pre-training, we collect a dataset called **Streetscape1M** based on the Global StreetScapes dataset [29]. Figure 5 illustrates the dataset construction process of **Streetscape1M** which can be divided into three steps:

1. **Study Area Selection:** As shown in Figure 5 (a), we sample 1 million street view images in the Global StreetScapes dataset across 688 cities globally.
2. **Remote Sensing Image Data Collection:** For each city, as shown in Figure 5 (b), we define the spatial scope and temporal scope of the study area and download Sentinel-2 multispectral remote sensing images based on the defined spatial and temporal scope.
3. **Geospatial Alignment Among Data Modalities:** As shown in Figure 5 (b), based on the spatial footprints of the collected overhead RS images and street view images, we establish their geospatial alignment between them and make them ready for GAIR model pre-training.

B.2. Baselines

To comprehensively evaluate GAIR, for the street view image encoder, we compare it against multiple baselines spanning geo-foundation models, general vision models, and self-supervised learning frameworks. Our baseline models are categorized as follows:

Geo-Foundation Models. These models are specifically designed for geospatial image prediction, leveraging pre-training strategies tailored to remote sensing and multimodal spatial data.

- **SatMAE** [15] – A transformer-based masked autoencoder pre-trained on large-scale remote sensing imagery, leveraging self-supervised learning to extract generalized spatial features.
- **CROMA** [20] – A contrastive learning model designed for multimodal geospatial representation learning, incorporating spatially-aware feature alignment.
- **PIS** [1] – A geospatial self-supervised pretraining approach that integrates intra-instance similarity.

General Vision Models. These models serve as broad benchmarks by assessing the performance of standard vision pretraining techniques when applied to geospatial tasks.

- **ImageNet Initialization** – ViT pre-trained on ImageNet using standard self-supervised training.
- **Random Initialization** – A control setting where models are trained from scratch without any pretraining.

Self-Supervised Learning Models. These models leverage contrastive and masked image pretraining paradigms to learn generalizable representations without labeled supervision.

- **MoCo v3-ImageNet** – A ViT trained on ImageNet using MoCo v3.
- **MAE-ImageNet** – A ViT trained on ImageNet using a masked autoencoder (MAE) objective [27].
- **MoCo v3-StreetScapes** – A ViT model pre-trained on Global StreetScapes data, capturing scene-level geospatial information using MoCo v3.
- **MAE-StreetScapes** – A ViT model pre-trained on Global StreetScapes using MAE.

B.3. Ablation settings

To further analyze the contribution of key components in GAIR, we design two ablation settings:

- **GAIR-MAE** – In this setup, we adopt a Masked Autoencoder (MAE) pretraining strategy [27] in place of GAIR’s contrastive learning objective. Here, the model learns to reconstruct missing image patches by treating the street view image as a masked region of the remote sensing image. Figure 6 provides a detailed visualization of this approach.

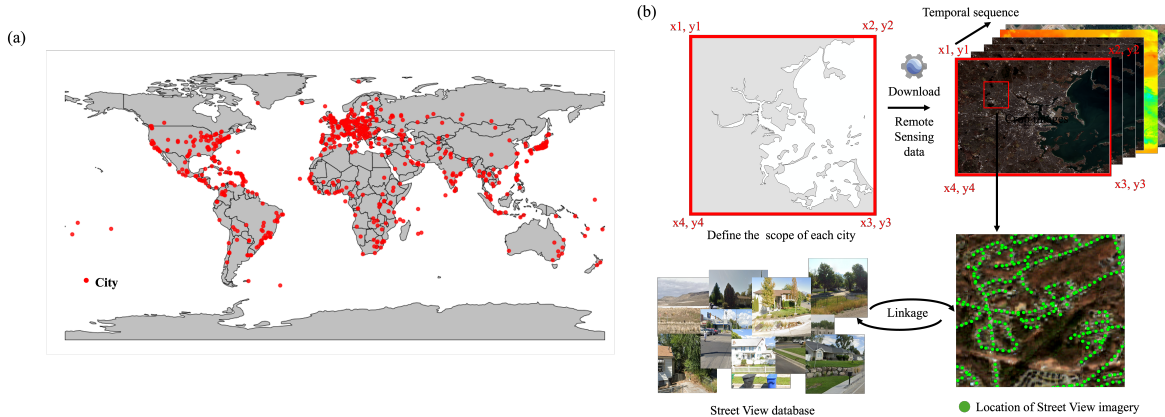


Figure 5. An illustration on the pipeline to construct our **StreetscapeIM** GeoFM pretraining dataset.

- **GAIR w/o Loc** – To assess the significance of geolocation encoding, we remove the location embedding $e(x_i)$ from GAIR.

B.4. Benchmark Details

To comprehensively evaluate the performance of GAIR, we construct multiple benchmark tasks spanning street view imagery, remote sensing data, and geolocation-based predictions. The details of each benchmark are as below.

B.4.1. Street View Imagery Tasks

These tasks use ground-level imagery to predict socio-economic indicators, human perception metrics, and image metadata.

- **Socio-Economic Indicator Regression:** This task is predicting ten socio-economic indicators using 410,286 street view images from Los Angeles and Boston. The indicators include population density, educational attainment (percentage of people with a bachelor’s degree or higher), health condition rates, racial demographics (percentage of people of color), median household income, proximity to public transportation, percentage of people who walk or bike, proportion of the population over 65 years old, crime rates, and visible sky area.
- **Human Perception Regression:** Using labels from the Global Streetscapes dataset [29], this task predicts human perception ratings for six attributes—'Beautiful', 'Boring', 'Depressing', 'Lively', 'Safe', and 'Wealthy'. These scores range from 0 to 1 and capture subjective assessments of urban environments.
- **View Direction Classification:** This classification task, based on the Global Streetscapes dataset, involves predicting the viewing direction of a street view image. The dataset provides two labels: "Front/Back" and "Side."
- **Imaging Platform Classification:** This task classifies the type of imaging platform used to capture a street view image, using labels from the Global Streetscapes dataset.

There 6 classes including driving surface, walking surface, cycling surface, tunnel, open fields, and railway.

B.4.2. Remote sensing tasks.

These benchmarks evaluate the performance of models on various remote sensing-based tasks.

- **Burn Scars Estimation:** This task uses the HLS Burn Scars dataset [34], which contains Sentinel-2 imagery of burn scars with burn scars masks for the years 2018-2021 in the United States. The dataset contains 804 scenes, each of size 512×512 pixels with six spectral bands (Blue, Green, Red, NIR, SW1, SW2). The masks contain a single band, where pixels labeled 1 represent burn scars, and 0 indicate unaffected areas. The dataset is randomly split into 2/3 for training and 1/3 for validation.
- **Crop Type Mapping (South Sudan):** This task uses a crop-type semantic segmentation dataset from South Sudan [41], based on Sentinel-2 imagery from 2017. The dataset covers 837 agricultural fields and includes four crop types. Each Sentinel-2 image is of 64×64 pixels and consists of 10 spectral bands (B2-B8, B8A, B11, and B12).
- **Cropland Boundary Delineation:** We employ the AI4SmallFarms dataset [56] for cropland boundary detection. This dataset includes 439,001 manually annotated agricultural field polygons distributed across 62 non-overlapping tiles. Each tile is derived from Sentinel-2 imagery, utilizing four spectral bands (B2, B3, B4, and B8) for delineation.

B.4.3. Location-Based Tasks

These benchmarks incorporate both geolocation information and remote sensing imagery to evaluate geospatial representation learning.

Image Regression For image regression tasks, we mainly use the MOSAICS dataset [59, 78], which provides large-

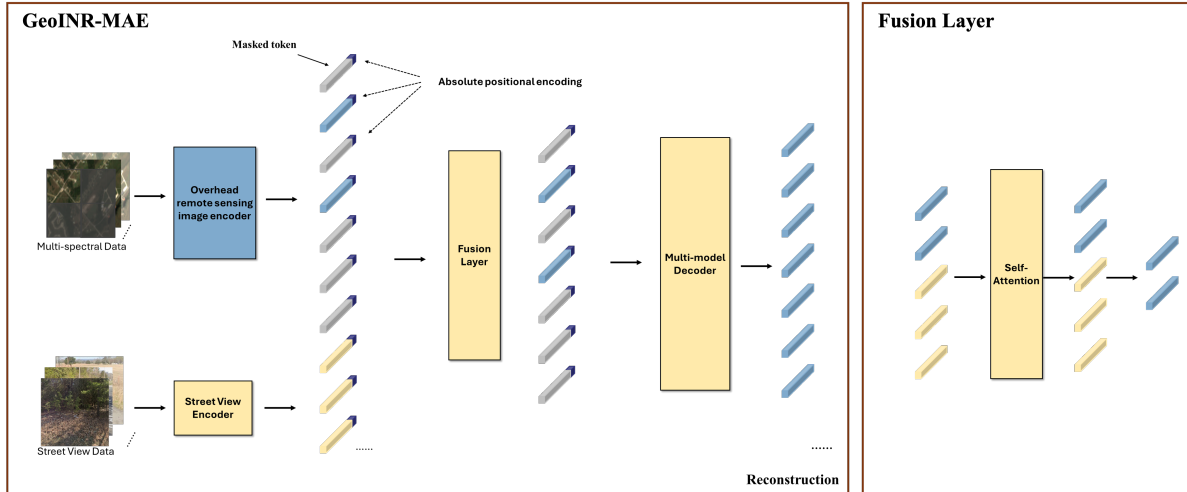


Figure 6. The architecture of one ablation setting, GAIR-MAE. In this variant, feature representations are extracted independently using two encoders, producing separate patch embeddings for remote sensing and street view modalities. Modality fusion is performed via a self-attention mechanism applied to both sets of patch embeddings. Finally, a masked autoencoder (MAE) decoder processes the fused representation to compute the reconstruction loss between the reconstructed masked regions and the input remote sensing images.

scale geospatial observations. The specific tasks include:

Population Density: This task estimates population density from daytime satellite imagery using the MOSAIKS dataset. The dataset originally consists of 100,000 records, but after preprocessing, we retain 425,637 geographically distributed samples. A log transformation is applied to normalize zero-valued cases. **Forest Cover:** Leveraging remote sensing data, this task predicts the percentage of land covered by forests, defined as vegetation exceeding 5 meters in height. The dataset includes 498,106 observations globally. **Nightlight Luminosity:** This task utilizes nighttime satellite images to predict the average radiance at night, as measured by the Visible Infrared Imaging Radiometer Suite (VIIRS) in 2015. The dataset contains 492,226 observations. **Elevation:** Using remote sensing RGB bands, this task predicts elevation levels based on data from the Shuttle Radar Topography Mission (SRTM) at NASA’s Jet Propulsion Laboratory (JPL) and other sources. The MOSAIKS dataset provides 498,115 elevation records.

Species Recognition Species recognition aims to classify images of different animal species using location-aware datasets. We include four datasets for evaluation: **Bird-Snap:** A dataset focused on bird species in North America, BirdSnap [7] contains 19,567 images across 500 species, with geolocation annotations provided by Mac Aodha et al. [42]. **NABirds:** NABirds [67] includes 23,699 images spanning 555 bird species from North America. The location information is derived from the eBird dataset [63], which aggregates citizen-science bird observations. **iNat2017:** This dataset, sourced from the iNaturalist 2017 challenge [68],

contains 675,170 images across 5,089 species categories. Each image is associated with a location, covering global regions. **iNat2018:** Similar to iNat2017, this dataset is part of the iNaturalist 2018 challenge [68], featuring 461,939 images across 8,142 species categories. It has a similar global distribution and data structure.

Flickr Image Classification For general image classification with geolocation metadata, we use the **YFCC100M-GEO100** dataset (YFCC) [77]. This dataset contains 88,986 geotagged images spanning 100 everyday object categories.

B.5. Implementation Details

Model Pretraining. We train our model on a Linux server equipped with 4 NVIDIA RTX A6000 GPUs (48GB). The training is conducted with a batch size of 256, a base learning rate of 1.5×10^{-6} , and a warm-up of the first 5% of total epochs. We apply two types of data augmentations: (1) standard augmentations for both Sentinel-2 imagery and street view images, including random horizontal flipping and color jittering, and (2) temporal augmentation for Sentinel-2 imagery, where images from different timestamps are randomly selected. We use the AdamW optimizer with $\beta_1 = 0.9$, $\beta_2 = 0.999$, and a weight decay of 0.01. For all baselines and GAIR, we utilize the ViT-B architecture.

Model Fine-Tuning. In this work, we evaluate GAIR across three benchmarks: street view imagery benchmarks, remote sensing imagery benchmarks, and location benchmarks.

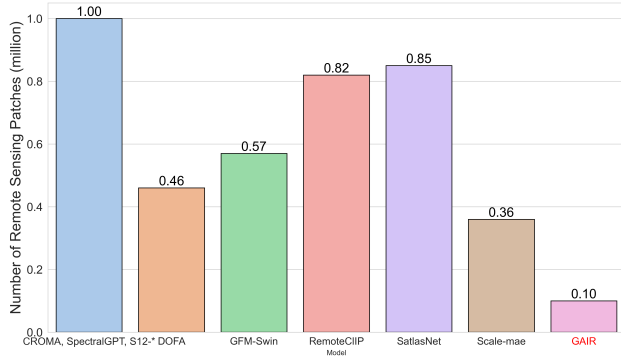


Figure 7. Comparison of the number of remote sensing patches used during model pretraining.

For street view imagery benchmarks, we apply three fine-tuning strategies to adapt the pretrained model to downstream tasks: 1) *Linear probing*: The encoder remains frozen, and only a single-layer MLP head is fine-tuned. 2) *Non-linear probing*: The encoder remains frozen, while the head consists of two MLP layers with a sigmoid activation function. 3) *Full fine-tuning*: All model parameters, including the encoder, are fine-tuned. For remote sensing imagery benchmark, we evaluate the representation quality of the pretrained models by evaluating them with frozen encoders without further fine-tuning. For location benchmarks, given the smaller capacity of the location encoder, we use the pretrained model as parameter initialization and then perform full fine-tuning to evaluate its performance. All baselines follow the same experimental setup, the batch size is of 256, 50 training epochs, learning rate of 1×10^{-3} and all images are resized to match the input requirements of each baseline model.

We implement street view baselines ourselves, remote sensing baselines using PANGAEA-Bench [51], and location baselines using TorchSpatial [74].

B.6. The Comparisons of Remote Sensing Training Samples in different GeoFMs

Figure 7 presents a comparative analysis of the number of remote sensing patches utilized during pretraining across various GeoFMs. Notably, GAIR is pretrained with only 0.1 million samples, significantly fewer than other models. Despite this reduced dataset size, GAIR achieves competitive performance, demonstrating the effectiveness of its joint training paradigm that integrates street view imagery with remote sensing data.

B.7. Reconstruction Loss and Contrastive Loss

Existing GeoFMs primarily adopt two pretraining objectives: reconstruction loss [2, 15, 20, 28, 76] and contrastive loss [28, 32]. To investigate the effectiveness of these approaches, we introduce an ablation setting where the model learns to reconstruct missing image patches by treating the street

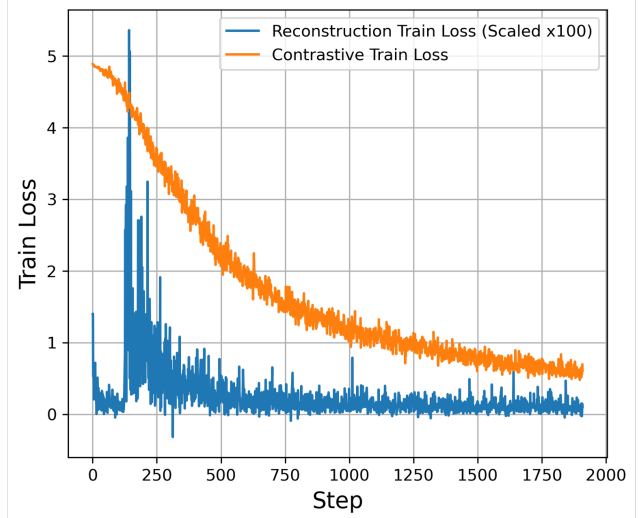


Figure 8. The loss curve of GAIR-MAE and GAIR during model pretraining.

view image as a masked region of the remote sensing image (Figure 6 in Appendix B.3). However, we observe that during pretraining, the loss remains unstable (Figure 8), ultimately leading the model to perform worse in downstream tasks.

B.8. More Visualization Results of Spatial Alignment

Figure 9 and 10 show more visualization results of spatial alignment.

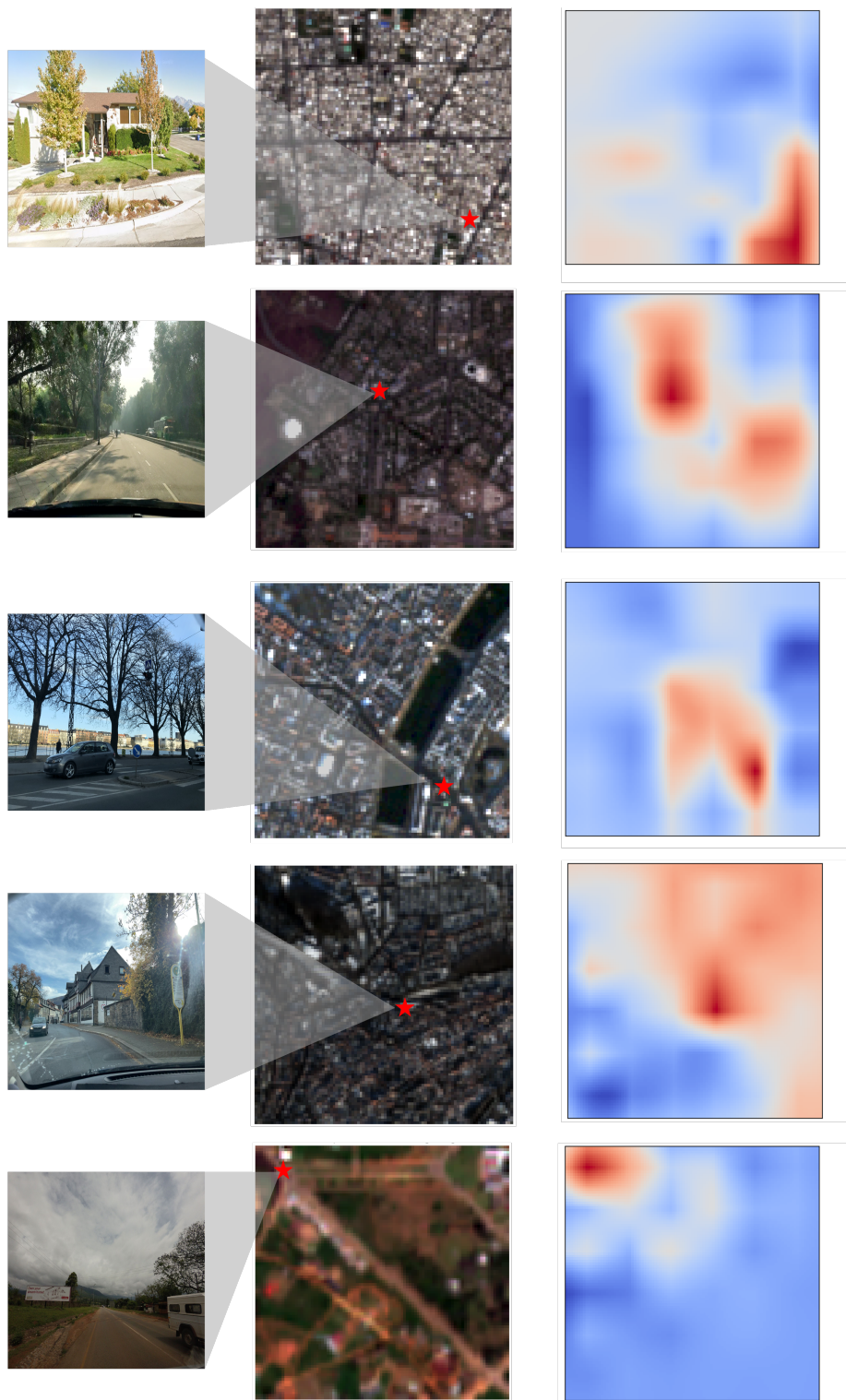


Figure 9. More results of cosine similarities between a SV image embedding $g(s_i)$ and different localized RS image embeddings $z_i^{(q)}$. The spatial scale of the similarity map is 100×100 pixels

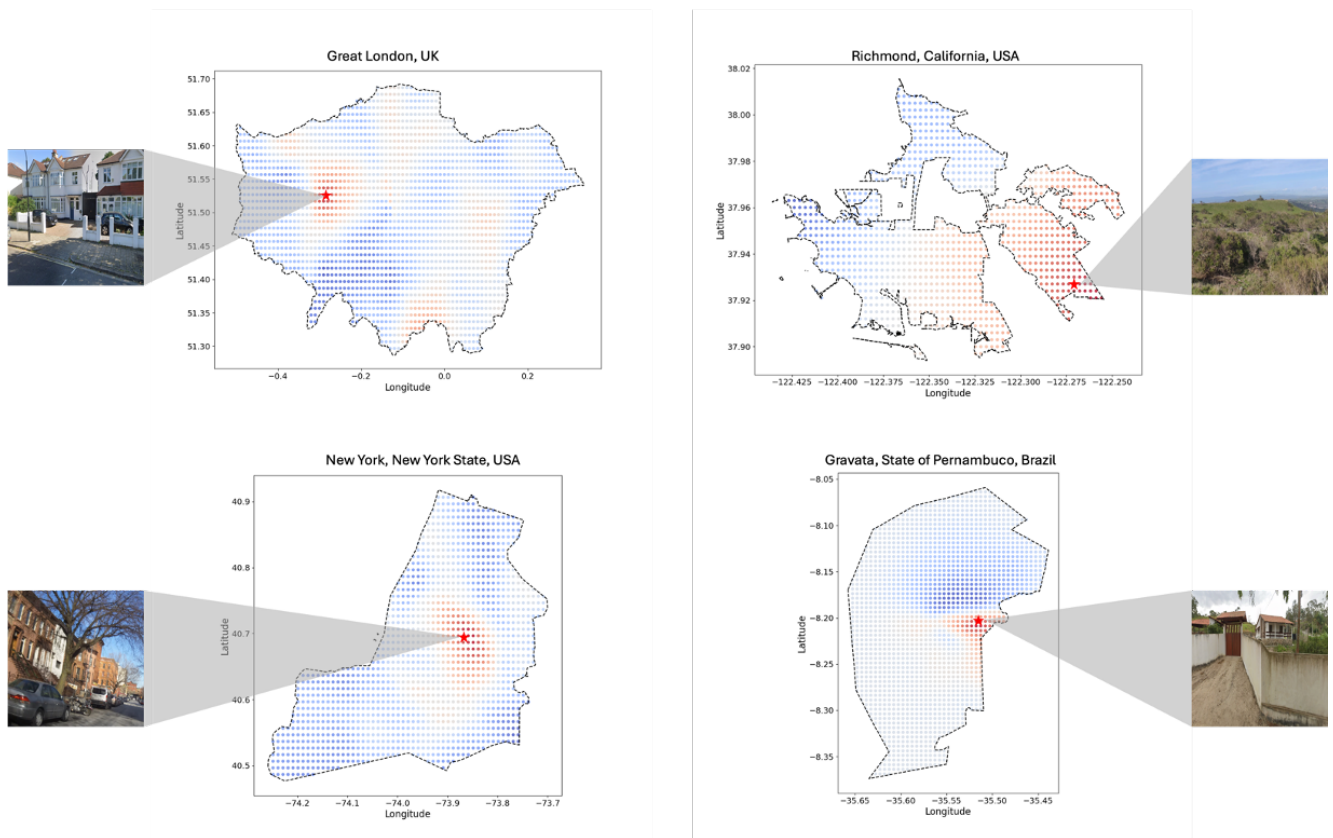


Figure 10. More results of cosine similarities between a SV image embedding $g(s_i)$ and location embeddings $e(x_i)$.